Neutron Emission Profile Measurement and Fast Charge Exchange Neutral Particle Flux Measurement for Transport Analysis of Energetic Ions in JT-60U

Masao ISHIKAWA, Takeo NISHITANI, Yoshinori KUSAMA, Atsuhiko SUKEGAWA, Manabu TAKECHI, Koji SHINOHARA, Anatoli KRASILNIKOV[1)], Yuri KASHUCK[1)], Mamiko SASAO[2)], Mitsutaka ISOBE[3)], Mamoru BABA[2)] and Toshio ITOGA[2)]

Japan Atomic Energy Agency, Naka 319-0193, Japan
[1)]*Troitsk Institute of Innovating and Fusion Research, Troitsk, Moscow region 142092, Russia*
[2)]*Department of Engineering, Tohoku University, Sendai 980-8578, Japan*
[3)]*National Institute for Fusion Science, Toki 509-5292, Japan*

(Received 10 November 2006 / Accepted 8 March 2007)

This paper describes diagnostics for transport analysis of energetic ions in JT-60U. Line integrated neutron emission profiles are measured using Stilbene neutron detectors, which are installed as a neutron emission profile monitor. The flux and energy distribution of charge exchange neutral particles are measured using a natural diamond detector (NDD). These measurements in the presence of bursting instabilities in the frequency range of Alfvén Eigenmode induced by negative-ion-based neutral beam injection, which are called Abrupt Large-amplitude Events, indicate that energetic ions are transported from the core region in the plasma due to a resonance interaction between energetic ions and the instabilities. Development of a digital signal processing (DSP) system for a neutron detector and a NDD enabling a sampling rate in the MHz class is proceeding. The DSP system for the neutron detector successfully discriminates between neutrons and gamma-rays in tests using neutron/gamma-ray sources.

Keywords: tokamak, JT-60U, negative-ion-based neutral beam, energetic ion, neutron, neutron profile measurement, natural diamond detector, neutral particle flux, Alfvén eigenmode, digital signal processing

DOI: 10.1585/pfr.2.019

1. Introduction

Burning plasmas are self-sustained by heating by 3.5 MeV alpha particles produced from DT fusion reactions. Alpha particles transfer their energy mostly to thermal electrons, which in turn heat plasma ions through collisions. For efficient plasma heating, it is important that energetic alpha particles are confined for a longer time than their slowing down time. However, poor confinement of the energetic alpha particles may be caused either by ripple loss [1] or by anomalous transport due to Magnetohydrodynamics (MHD) instabilities such as Alfvén Eigenmodes (AEs) [2]. Such losses of alpha particles can not only reduce the plasma heating efficiency, but also lead to excessive heat loading and damage to the first wall and/or the divertor plate structure. Therefore, understanding of energetic alpha particle confinement in the presence of MHD instabilities is a very important issue for ITER [3].

In present tokamak devices, such as JT-60U [4], JET [5] and DIII-D [6], studies for this issue have been performed using energetic particles introduced by neutral beam injection (NBI) or produced by ion cyclotron range of frequency (ICRF) heating, instead of alpha particles. Neutron diagnostics is one of the most important diagnostic methods to know energetic ion behavior, not only in present devices but also in future devices like ITER, because neutrons emitted from the plasma provide information on energetic ions. Information on energetic ion confinement also appears in their energy distribution. Since charge exchange (CX) neutral particles emitted from the plasma have information on the energy distribution function of confined energetic ions, energy distribution and flux measurements of CX neutral particles are also very important to investigate behavior of energetic ions.

In JT-60U, energetic ion experiments in the ITER relevant parameter regime of $\langle\beta_h\rangle$ (volume-averaged energetic ion beta) $\sim 0.1\%$ can be performed using the negative-ion-based NB (NNB) injection [7], which can produce energetic ions of 300 - 420 keV in the toroidal direction. Recently, energetic ion transport due to AEs induced by NNB injection has been extensively studied. In particular, bursting modes with large amplitude in the frequency range of TAEs, which are called Abrupt Large-amplitude Events (ALEs), have been observed [8, 9] in JT-60U weak shear plasmas, and it is considered that ALEs can induce large transport of energetic ions. At present, in order to ana-

author's e-mail: ishikawa@jaea.go.jp

lyze characteristics of energetic ion behavior upon occurrence of ALEs, the total neutron emission rate is measured with a fission chamber [10]. The CX neutral particle flux is also measured with an E//B type neutral particle analyzer (E//B NPA) [11]. When ALEs occur, reduction of the total neutron number is observed, which suggests confinement degradation of energetic ions [8, 9]. However, since the total neutron emission rate is a volume-integrated value, it is not yet understood how energetic ions are transported in the plasmas and whether energetic ions are lost from the plasmas. On the other hand, the rapid increase in CX neutral particle fluxes induced by ALEs is observed. The energy dependence of the enhanced neutral particle flux suggests the resonant interaction between energetic ions and ALEs as a cause of the enhanced transport of energetic ions [8, 9]. However, it is not clearly understood yet, because the energy distribution of CX neutral particles measured using the E//B NPA is discrete and the distribution in the low energy range of less than 160 keV could not be obtained.

In the present study, to overcome these problems, two kinds of measurement system have been developed. One is a measurement system of neutron emission profile. A neutron emission profile provides not only the birth profile of alpha particles in DT plasmas [12] but also information on the radial profile of energetic ions in DD plasmas [13]. Therefore, this measurement can be used to investigate how energetic ions are transported in DD plasmas such as in JT-60U experiments. In order to measure only neutrons in the neutron/gamma mixture field in JT-60U experiments, Stilbene neutron detectors (SNDs) are applied. A SND has a good neutron/gamma discrimination property and the size is compact. Therefore, it can be installed to the detector box of the neutron emission profile monitor without any additional modules for discrimination between neutrons and gamma-rays. The other one is a measurement system of CX fast neutral particle flux and energy distribution with a natural diamond detector (NDD) [14, 15]. A NDD provides continuous energy distribution of CX neutral particles with high energy resolution. Therefore, it is possible to investigate which energy region of energetic ions is affected due to MHD instabilities in detail.

In this paper, the development of these measurement systems is reviewed and the results of transport studies of energetic ions using these measurements are reported. The development of the measurement system of neutron emission profile using SNDs is described in Sec. 2. The results of the energetic ion transport study are also mentioned. In Sec. 3, we present the measurement system of CX neutral particles using the NDD. Furthermore, the results of the measurement of fast neutral particle flux and energy distribution for plasmas with instabilities are reported. Upgrade of the maximum count rate of the SND and the NDD using a digital signal processing technique, which is applicable to ITER, is discussed in Sec. 4. Finally, a summary is presented in Sec. 5.

2. Measurement of Neutron Emission Profile in JT-60U

2.1 Instrument of neutron emission profile measurement

Figure 1 shows a neutron emission profile monitor in JT-60U [16]. It is comprised of a six channel collimator array (2.6 m × 1.3 m × 1.6 m) viewing a poloidal cross section of the plasma, about 5 m away from the plasma center. Since the penetration length of neutrons in materials is very large, such a large neutron collimator is needed in order to measure neutron emission profiles. The sight line of each collimator channel is constrained by the space available in the JT-60U torus hall. As illustrated in Fig. 1, the sight line of one of the 6 collimator channels passes through the center (R = 3.3 m, z = 0 m) of the vacuum vessel, and the others are oriented along off-axis chords. The covered area is the lower half of the poloidal cross section of the plasma. The structure of the neutron collimator array is illustrated in Fig. 2. The collimator array utilizes Polyethylene assemblies to shield against neutrons out of the sight line of each channel. Lead reduces flux of 2.2 MeV capture gamma-rays generated by neutrons incident to the Polyethylene assemblies and backscattered gamma-rays emitted from the external structures of the JT-60U device. The housing of the neutron detector is surrounded by soft magnetic iron to remove the influence of the magnetic field. The size and the solid angle of each collimator tube are 30 mm$^{\Phi}$× 800 mm^{L} and about 1 × 10^{-3}, respectively, where Φ and L are the diameter of the aperture and the length of the collimator, respectively. The viewing extent channel at R = 3.3 m of each collimator is

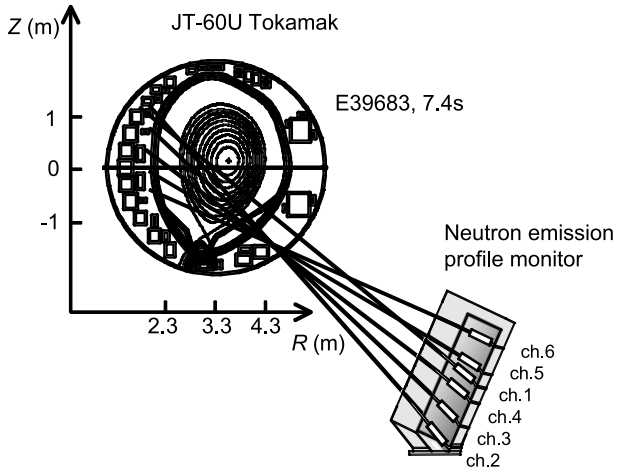

Fig. 1 Illustration of the JT-60U neutron-emission-profile monitor and its collimation geometry. The plasma configuration at t = 7.4 s in the E39683 shot is illustrated. The line-of-sight chords are shown in the viewing poloidal cross section of the plasma. The innermost channel (ch.1) passes through $r/a \sim 0.25$, and the channels from the 2nd to the 6th passes through $r/a \sim 0.39$, 0.52, 0.61, 0.76 and 0.86, respectively.

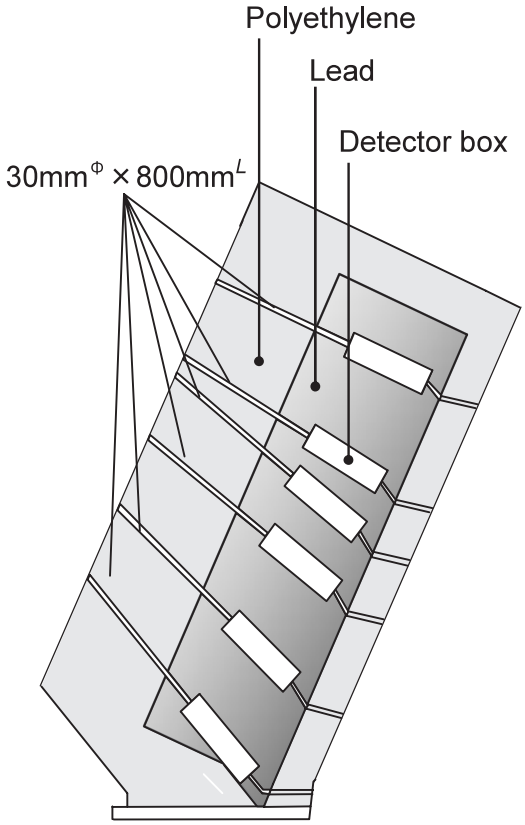

Fig. 2 A schematic structure of 6 channel neutron collimator array.

about 300 mm. We can change the aperture size of the collimator channel to 20 mm$^{\Phi}$, 15 mm$^{\Phi}$, 12 mm$^{\Phi}$ and 10 mm$^{\Phi}$ depending on the experimental condition. Then, the viewing extent is changed to about 200 mm, 150 mm, 120 mm and 100 mm, respectively.

2.2 Stilbene neutron detector

A neutron detector is needed to discriminate neutrons from background gamma-rays in the neutron/gamma mixture field in JT-60U experiments. At first a NE213 liquid organic scintillator, which is commonly used as a neutron detector, had been used, because of its good time resolution and well-known efficiency. But such an organic scintillator is sensitive not only to neutrons but also to gamma-rays. In order to detect neutrons only, another module set for discriminating gamma-ray is necessary. Moreover, the set is relatively complicated and a wide space is needed because the number of the collimator channels is six.

In the present study, a Stilbene neutron detector (SND), developed by TRINITI laboratory in Russia recently, replaced the NE213 scintillator. The SND can measure only neutrons without any additional modules. It also can be installed in the detector box of the neutron emission profile monitor since the size is compact (70 mm$^{\Phi}$× 400 mm^{L}). The structure of the SND is shown in Fig. 3. It

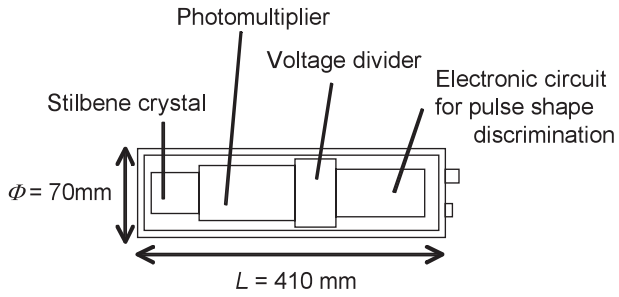

Fig. 3 A schematic structure of a Stilbene neutron detector. The Stilbene neutron detector consists of a Stilbene scintillator and an electronic circuit for discrimination between neutrons and gamma-rays.

consists of a Stilbene crystal scintillator [17] and an electronic circuit which discriminates between neutrons and gamma-rays. A Stilbene crystal is used as the scintillation material since it has excellent discrimination property through the generated pulse shape. It allows discrimination between the scintillation induced by charged particles scattered by neutrons and that by electrons energized by gamma-rays. The SND has two outputs. One is LINEAR output, which provides unipolar pulses with the peak amplitude linearly proportional to the energy of the detected neutrons or gamma-rays. The other is CONTROL output, which provides an Emitter Coupled Logic (ECL) signal when a neutron with the energy beyond the threshold E_{thr} is detected. Here E_{thr} is determined by adjusting the electronic circuit. In the JT-60U experiments, we count ECL signals from the CONTROL output to measure neutron flux. The absolute neutron detection efficiency for the SND was determined from calibration with DD neutrons from the Fusion Neutron Source (FNS) in JAEA Tokai [18]. High intensity DD neutron flux can be produced by directing accelerated 400 keV deuterons into a deuterium gas target.

2.3 Correction to the experimental data

Since some fusion neutrons are attenuated when they pass through the structural material of the vacuum vessel, correction for this attenuation is required for absolute neutron flux measurement. It is also necessary to consider the effect of neutron scattering not only at the structural material but also at the collimator walls. A neutron transport code called the Monte Carlo code for Neutron and Photon Transport (MCNP) [19] is used to estimate these correction factors. To carry out calculations using the MCNP code, a geometric configuration of the system is necessary. Then, calculations were carried out for a system which consists of only the vacuum vessel of JT-60U and the neutron emission profile monitor. As a result, it was found that a large number of scattered and attenuated neutrons have energy less than 1 MeV. Therefore, the threshold energy of CONTROL output of the Stilbene neutron detectors are deter-

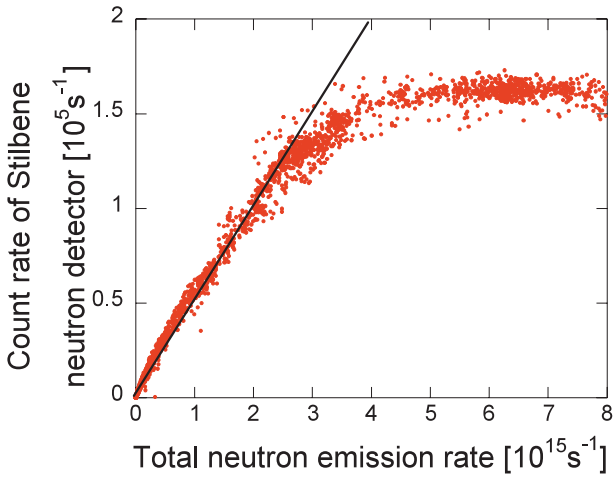

Fig. 4 The relation between the count rate of the Stilbene neutron detector and the total neutron emission rate.

mined as E_{thr} = 1 MeV. Also, we corrected the effects of attenuated and scattered neutrons over 1 MeV in actual measurements [16].

2.4 Linearity of the count rate of the Stilbene neutron detector in JT-60U experiments

The count rate of the SND is restricted by the gate integration time of the discrimination circuit. The maximum count rate of neutrons also depends on the sum of neutron flux and gamma-ray flux because the Stilbene scintillator itself is sensitive to gamma-rays. Therefore, we need to confirm the linearity of the count rate of the SNDs. Figure 4 shows the relation between the count rate of the SND whose sight line passes through the plasma axis and the total neutron emission rate measured with the fission chamber. One can see that the linearity of the count rate is deviated from the total neutron emission rate of about 3 $\times$ 10^{15} n/s. This comparison indicates that the maximum count rate of the SND is about 1 - 1.3 $\times$ 10^5 counts/s (cps). For this reason, it is necessary that the aperture size of each collimator tube is selected in order not to exceed the maximum count rate.

2.5 Measurement of neutron emission profile in quiescent plasmas

Here, a representative result of measurements of neutron emission profile in quiescent plasmas is presented. Figure 5 shows waveforms of a typical ELMy H-mode plasma. Here, the plasma current (I_p) is 1 MA and the toroidal magnetic filed (B_T) is 2.0 T. Significant instabilities are not observed in the core plasma region throughout this discharge. The plasma configuration at t = 7.4 s is shown in Fig. 1. The sight line of the innermost channel extends to r/a ~ 0.25, and that of the outermost channel extends to r/a ~ 0.86, where r/a is the normalized minor radius.

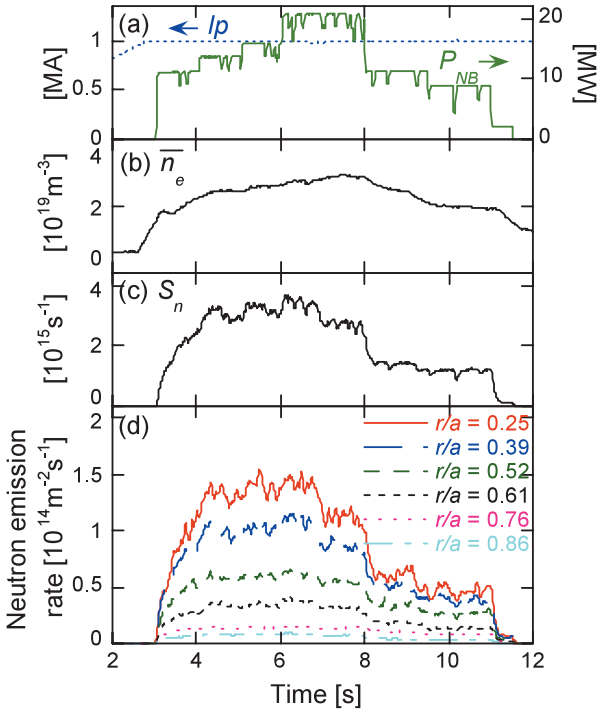

Fig. 5 The waveforms of an ELMy H-mode plasma. (a) The plasma current (I_P) and the injected beam power (P_{NB}), (b) the line-averaged electron density ($\overline{n_e}$), (c) the total neuron emission rate (Sn) and (d) the neutron emission rate at the various chords.

Neutron signals during neutral beam injection are shown in Fig. 5 (d). The data of Fig. 5 (d) are derived by taking the geometry factor into account, and the sampling frequency period is set at 10 ms. The signal of the innermost channel is the largest.

Figure 6 shows a measured line-integrated neutron emission profile (circles) compared with the profile calculated using a transport code called TOPICS (squares) [20] in JT-60U at t = 7.4 s. In the calculation using the TOPICS code, the measured profile of the ion temperature (T_i (r/a)), the electron temperature (T_e (r/a)), the electron density (n_e (r/a)) are used. T_i (r/a) is measured by charge exchange recombination spectroscopy [21], n_e (r/a) and T_e (r/a) by Thomson scattering measurement [22]. Z_{eff} (r/a) is assumed to be constant in the plasma, and is evaluated using a profile of Bremsstrahlung [23]. Carbon was the dominant impurity in this discharge, and Z_{eff} is evaluated to be 2.9 at 7.4 s. The ionization source, injected neutral beam, is calculated, and then the density profile of beam component n_b is calculated using Stix's stationary solution for the velocity distribution function [24] in the TOPICS code. Ion density n_i is also given by $n_i = n_{th} + n_b$, where n_{th} is the thermal component. Then, the respective DD neutron profiles emitted by thermal-thermal (TH), beam-thermal (BT) and beam-beam (BB) reactions are calculated. In this calculation the component fractions of TH, BT and BB neutrons are 11%, 69% and 20%, respectively.

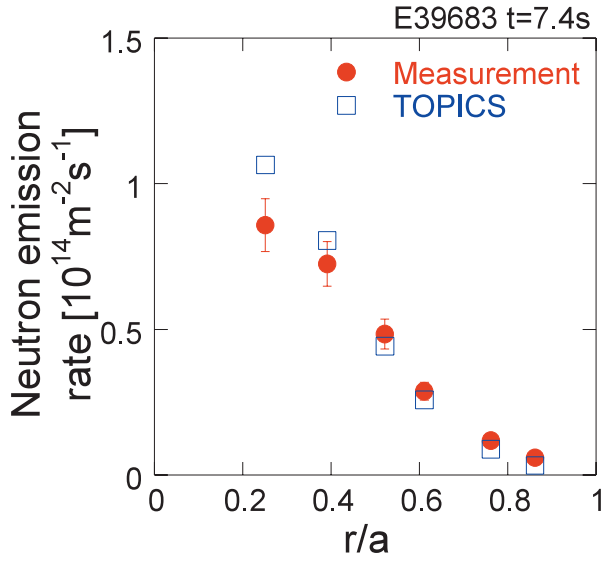

Fig. 6 The profile of the line-integrated neutron emission. Circles indicate the measured results by the Stilbene neutron detector and squares show the calculated results by the TOPICS code.

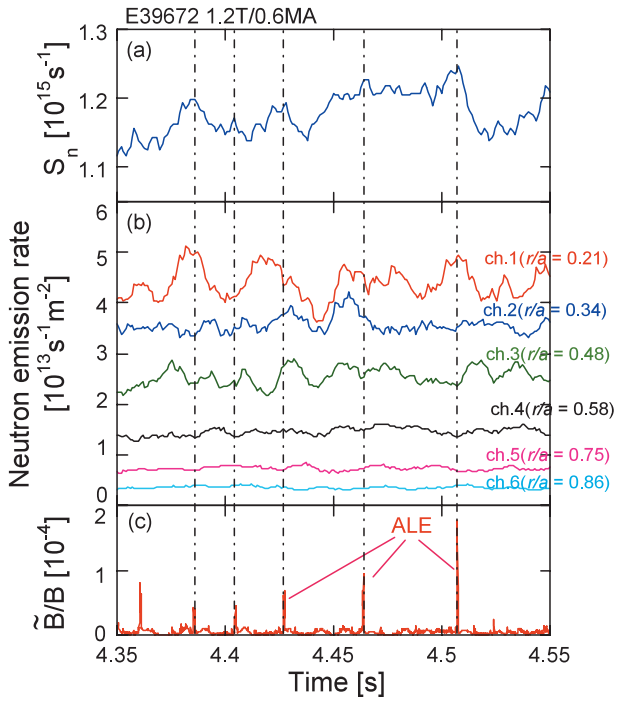

Fig. 7 The neutron signals during the occurrence of ALEs. (a) The total neutron emission rate. (b) The neutron signals from the neutron emission profile monitor. The signal of the innermost channel is the top. (c) The mode amplitude of the magnetic fluctuation.

In Fig. 6 the line-integrated total neutron (TH+BT+BB) signal along each sight line calculated by the TOPICS code is shown. Although there is 30% error in the innermost channel between the measurement and the calculation, there is an agreement within 10% in the other channels [16]. One of reason for this discrepancy in the innermost channel, where there are large amount of energetic ions produced by the neutral beam injection, could be due to the assumption of using Stix's stationary solution as the energetic ion velocity distribution function in the calculation.

Signal to noise ratio S/N is strongly dependent on the statistical error of each signal, which is fixed by the count rate of the SND of each collimator channel. Then, the sampling time and/or the aperture size of each collimator tube of the neutron emission profile monitor are selected in order that each statistical error is less than 10% and the count rate of each SND is not to exceed the maximum count rate. The sampling rate is set at 10 ms in usual experiments. The collimator size of the inner channels and the outer channels are also set at 20 mm and at 30 mm, which correspond to the spatial resolution of 200 mm and 300 mm at $R = 3.3$ m, respectively.

2.6 Transport analysis of energetic ions due to instabilities using neutron emission profile measurement

Shown in Fig. 7 is a typical result of AE experiments using the neutron emission profile measurement, where NNB is injected into weak shear plasmas ($I_P = 0.6$ MA, $B_T = 1.2$ T). In the resulting discharge, ALEs [8, 9] are observed as shown in Fig. 7 (c). An ALE has a time scale of 200 - 400 μs, and its amplitude rises up to $\delta B/B \sim 10^{-3}$ near the first wall. The total neutron emission rate decreases by 2 ~ 10% due to ALEs, as shown in Fig. 7 (a). Since neutrons produced via the beam-target ion reaction account for over 90% of the total neutron emission in this shot according to the TOPICS code calculation, and since the ion temperature and the electron density hardly changed, the observed change of the total neutron emission rate must be attributed to confinement degradation of energetic ions. Figure 7 (b) shows signals of each channel of the neutron emission profile monitor. The sampling frequency period is set at 2 ms during this discharge to investigate changes in each signal due to ALEs. In the diagram, each signal is labeled with the minimum normalized minor radius through which the sight line passed through. The neutron emission signals from the central region ($r/a < 0.34$) decrease after ALEs, while signals from the peripheral region ($r/a > 0.48$) increase after ALEs. Since the neutron emission rate shown in Fig. 7 (b) is the line-integrated one along each line of sight, we have to employ an Abel inversion method to obtain a radial neutron emission profile. The Wiener Filter method [25] was applied in the Abel inversion. Radial profiles of the neutron emission rate obtained by the Abel inversion before and after the occurrence of an ALE are shown in Fig. 8. One can see that the neutron emission rate in the center region significantly reduces due to ALE, while that in the

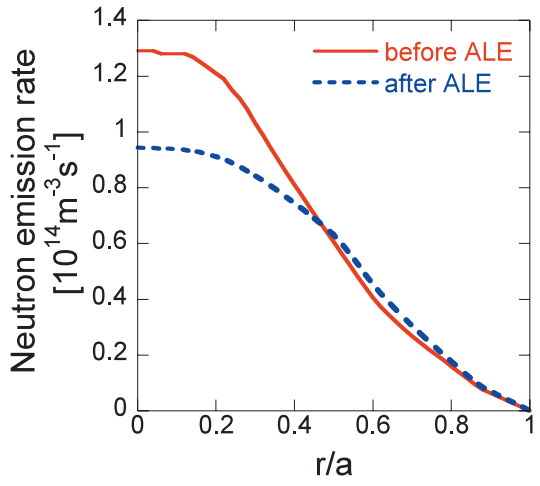

Fig. 8 The neutron emission profiles obtained by the Abel inversion before and after ALE at t = 4.51 s

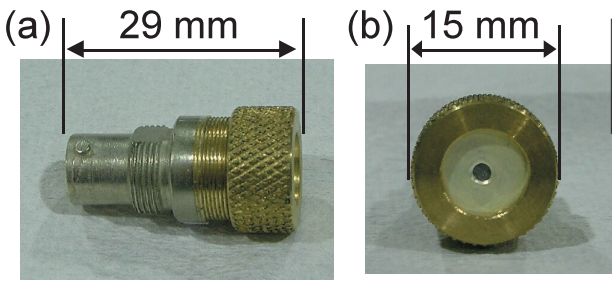

Fig. 9 Pictures of (a) the side view and (b) the front view of the NDD.

peripheral region slightly increases. Thus, energetic ion transport from the core region of the plasma to the outer region due to the ALE was discovered for the first time, from the measurement of neuron emission profiles [26].

3. Charge Exchange Neutral Particle Measurements with NDD

3.1 NDD as CX neutral particle spectrometer

An NDD [14, 15] has an electrode-semiconductor-electrode structure, where the electrodes are thin graphite contact layers and the semiconductor is made of pure natural diamond of group IIa. The NDD has many favorable characteristics as a radiation detector; very compact size (15 mm^{Φ} × 29 mm^{L}, shown in Fig. 9), high band gap (5.5 eV), high resistivity (> 10^{15} Ωm), high breakdown voltage (10^7 V/cm), large saturation velocity (2 × 10^7 cm/s), a free drift time (10 - 15 ns), and so on. Since the NDD produces signals which are proportional to the kinetic energy of incident neutral particles, it can operate as a spectrometer. The high band gap enables a NDD to operate at room temperature, unlike a silicon detector [27] (the band gap is ~1 eV) which needs cooling to operate. Also, compared with an artificial CVD diamond [28], the natural diamond of the NDD has very few crystal defects and impurities in it, resulting in high energy resolution. Thus the NDD has crucial advantages over other spectrometric detectors.

3.2 Installation of the NDD and the neutron and γ–ray shielding in JT-60U

The NDD has been installed along a tangential port with a tangent radius (R_{tan}) of 2.5 m to measure neutralized co-going beam ions. The pitch angle of neutral particles coming into the NDD are almost the same as that of the initial path of energetic ions injected by NNB (R_{tan} ~ 2.6 m). The distance between the NDD and the plasma axis is approximately 10 m.

The NDD is, however, sensitive to neutrons, gamma-rays and photon radiation such as UV rays and soft X rays. In particular, neutrons create much noise in the neutral particle measurement of deuterium plasmas in JT-60U experiments. The neutron flux at the NDD position is estimated in the following way. For simplification, we only consider a point source of DD neutrons at the center of the torus instead of neutrons emitted from the plasma. Here, we set the neutron yield Y_{n} to be 2 × 10^{15}, which is the typical neutron yield in JT-60U experiments. Since the distance between the point source and the NDD is ~13 m, the direct neutron flux at the detector position is estimated to be ~10^8 n/s. The sensitivity of the NDD to DD neutrons is ~10^{-3} count/(n/cm^2), which means that neutrons will have a background count rate of N ~10^5 cps. Since the maximum count rate of the present data acquisition system (Sec. 3.3) is ~2 × 10^5 cps, the NDD must be protected from neutrons in order to measure flux and energy distribution of CX neutral particles effectively. Also, since gamma-rays could cause much noise in the measurement of CX neutral particles, those should be removed. For this purpose, a neutron and gamma-ray (n-γ) shield has been set up around the NDD [29]. The n-γ shield was designed using the MCNP code to reduce neutron and gamma-ray background by at least 1 order. Figure 10 shows a schematic structure of the n-γ shields, whose size is 70 cm × 50 cm × 48 cm. As illustrated in Fig. 10, the n-γ shield consists of an inner layer of lead more than 5 cm thick and an outer wall of borated polyethylene more than 10 cm thick. The purpose of utilizing polyethylene and lead is the same as in the neutron emission profile monitor shown in Fig. 2. Moreover, the NDD is also covered by a stainless steel cylinder of 10 cm length in order to shield UV-rays and x-rays. Two stainless steel plates with an aperture whose diameter can be changed to ϕ =1, 3 or 5 mm are installed for control of CX neutral particle flux coming into the NDD as illustrated in Fig. 10. The viewing range at the plasma center is about 100 mm in the case of each steel plate having ϕ = 3 mm.

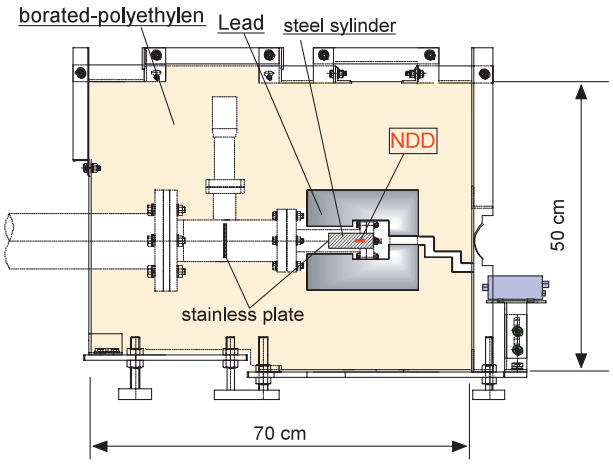

Fig. 10 A schematic structure of the n-γ shield. The NDD is mounted inside a stainless steel cylinder.

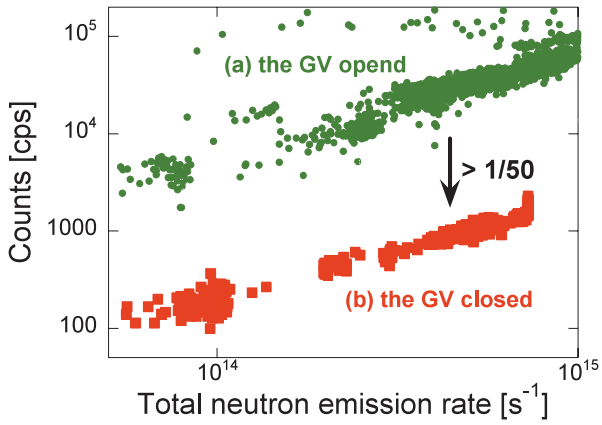

Fig. 11 The relation between the total neutron emission rate and the NDD counts in the case of (a) the GV opened (circles) and (b) the GV closed (squares).

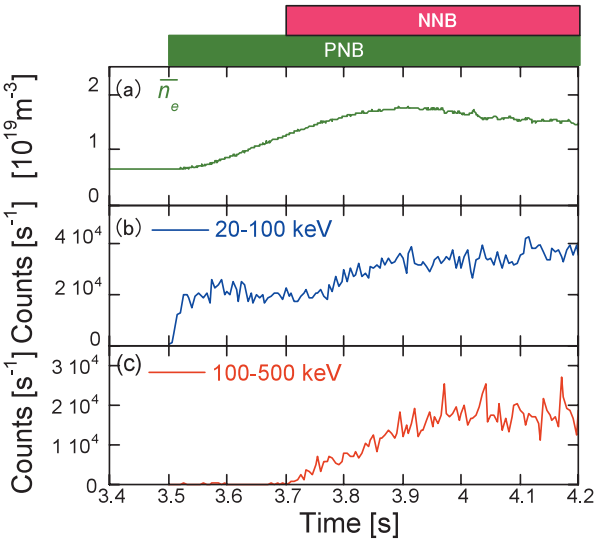

Fig. 12 The time traces of (a) the line-averaged electron density and (b) the CX neutral particle flux in the energy range (c) from 20 to 100 keV and (d) from 100 to 500 keV.

3.3 Data acquisition and energy calibration of the NDD

The data acquisition system for measurements of energy distribution and flux of CX neutral particles is as follows. The NDD is connected to a preamplifier (CANBERRA-2001A), then to a fast spectroscopy amplifier (CANBERRA-2024). Signals from the amplifier are fed to a fast analog to digital converter (CANBERRA-8715). The converted digital signal is fed through a router to a histogramming memory (TOYO629) to analyze pulse height spectra of neutral particles. The energy calibration is performed using a ^{241}Am alpha source (5.48 MeV) under almost the same conditions as in JT-60U experiments. Then, the energy channel relation is set to be 500 keV/256 Ch. (1.95 keV/ch.). The maximum count rate in the present system is about 2×10^5 cps. This is caused by pile up of signals from the fast spectroscopy amplifier. Then, the aperture sizes of two stainless steel plates are needed to select in order not to exceed the maximum count rate.

3.4 Measurement of fluxes and energy distribution of CX neutral particles in NB injected plasmas

The effects of DD neutrons, scattered neutrons and gamma-rays on the CX neutral particle measurement were checked. The check was performed using the gate valve (GV), which had been installed between the plasma and the NDD. The GV is usually open for measurements of CX neutral particles. However, if the GV is closed, CX neutral particles emitted from the plasma are stopped at the closed GV, while neutrons and gamma-rays are hardly affected. Therefore, the effects of neutron and gamma-ray background can be investigated by opening and closing the GV. Figure 11 shows the relation between the total neutron emission rate measured with the fission chamber and the count rate of the NDD in all energy channels. In Fig. 11, the group (a) corresponds to the count rate for the opened GV, which is the usual experimental setting. The group (b) corresponds to the count rate for the closed GV, which means the neutron and gamma-ray background noise. Comparing (a) with (b) in Fig. 11, the ratio of the signal (a) to the noise (b), S/N, is more than 50. Thus, the NDD with the n-γ shield is a reliable neutral spectrometer for the JT-60U deuterium plasmas.

Figure 12 shows time dependent variation of the line-averaged electron density and the CX neutral particle fluxes in two different energy ranges measured by the NDD, 20 - 100 keV and 100 - 500 keV, respectively, in the PNB and the NNB injected plasma. The injection energy of the PNB and the NNB was 85 keV and 387 keV, respectively. When the PNB was injected prior to the NNB, the CX neutral particle flux in the 20 - 100 keV range in-

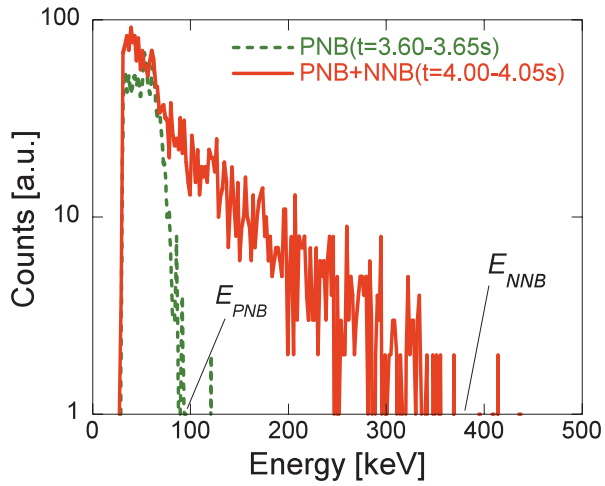

Fig. 13 The energy distributions of the CX neutral particles in the phase of the PNB injection only (the broken line) and in the phase of the PNB + NNB injection (the solid line).

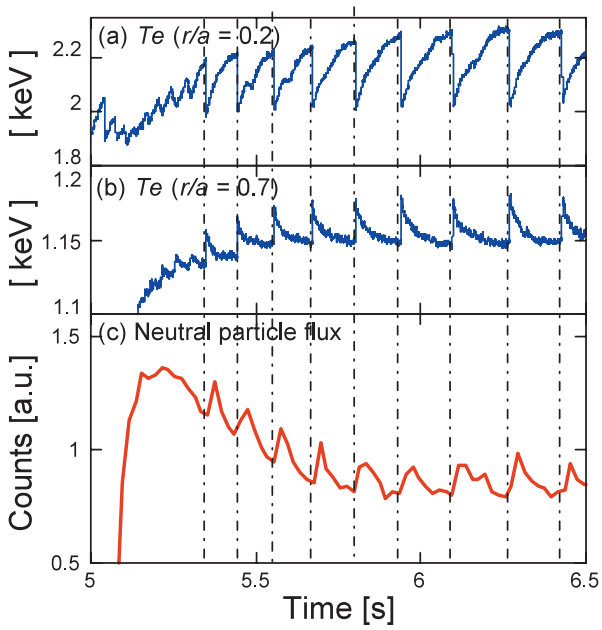

Fig. 14 The time traces of the electron temperature (a) at $r/a \sim 0.2$ and (b) at $r/a \sim 0.7$. (c) The time trace of the CX neural particle flux in energy range from 20 to 100 keV.

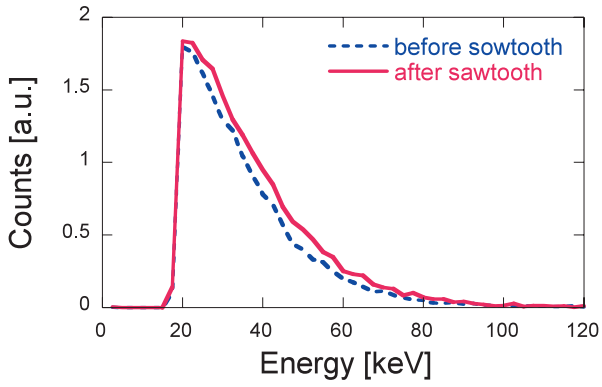

Fig. 15 The energy distributions of the CX neutral particles before (the broken line) and after (the solid line) the sawtooth.

creased, but the flux over 100 keV didn't increase. On the other hand, the flux over 100 keV started increasing when the NNB was injected. The energy distribution of CX neutral particles during the phase of the PNB injection only and during that of both PNB and the NNB injections are shown in Fig. 13. One can see that the energy distribution was significantly changed due to the NNB injection. The maximum energy in both distributions corresponds to the maximum energy of injected NBs. After the NNB was turned off, the slowing down of beam ions was also observed.

Signals in low energy range below 20 keV are dominated by electronic noise, which is mainly due to the preamplifier. Pulses of photon radiation such as UV-rays and soft x-rays are also produced in such low energy range. Therefore, signals with energy below 20 keV are eliminated by the lower level discriminator of the ADC.

Time resolved measurement of the continuous energy distributions of CX neutral particles in the energy range between 20 - 500 keV with energy resolution of 1.95 keV become possible using the NDD [29]. The data sampling frequency period is changed from 10 ms to 1 ms depending on the experimental conditions.

3.5 Fast CX neutral particle measurement for transport analysis of energetic ions

In a plasma with minimum safety factor value (q_m) of < 1, sawtooth oscillations of the temperature and the density are observed around the $q = 1$ surface due to magnetic reconnection [30]. The effect of sawtooth on the redistribution of energetic ions in tokamaks has been studied both experimentally [31] and theoretically [32]. Figures 14 (a) and (b) show the time traces of the electron temperature measured from the ECE measurement [33]. The sawtooth electron temperature variation in the center of the plasma as well as the inverted behavior which occurs in the outer region were observed. Figure 14 (c) shows the time trace of the CX neutral particle flux in the same discharge. Enhanced CX neutral particle fluxes are observed when sawtooth crashes occur. Figure 15 shows energy distributions of CX neutral particles before and after the occurrence of sawtooth crashes. The flux is enhanced in the entire energy range due to sawtooth oscillation. Since the energetic ions are neutralized through a CX reaction with the neutral particle D^0 or the hydrogen-like carbon ion C^{5+} in the outer region of the plasma, the enhancement of CX neutral particle flux indicates that there has been energetic ion transport from the core region to the outer region in the plasma. However, an increase in CX neutral particles is seen in the

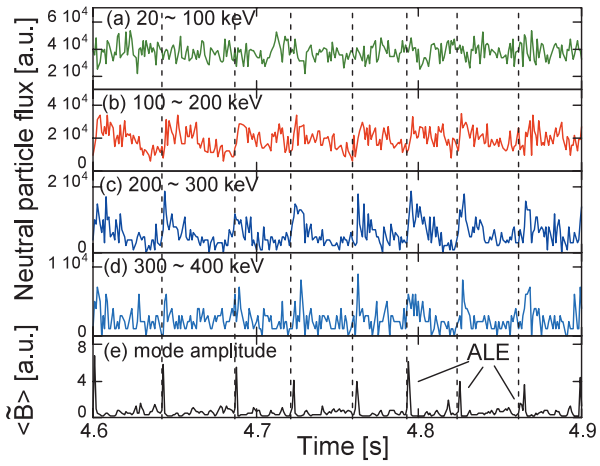

Fig. 16 The time traces of the CX neutral particle flux with the energy windows of (a) 20 - 100 keV, (b) 100 - 200 keV, (c) 200 - 300 keV and (d) 300 - 400 keV. (e) The time trace of the mode amplitude during the NNB injection in the E43014 shot.

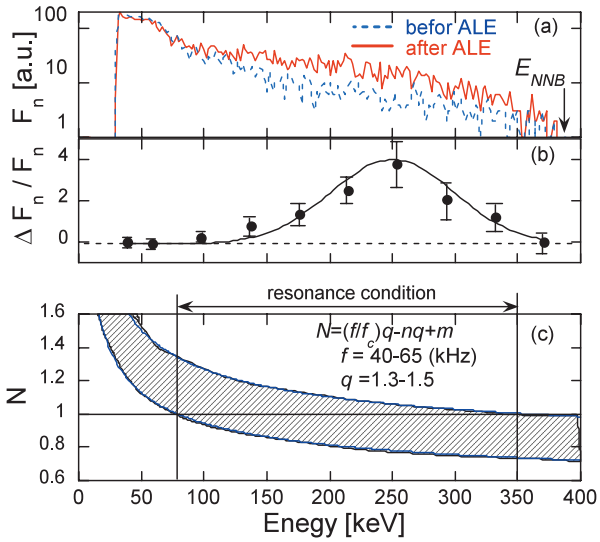

Fig. 17 (a) The energy distributions of the CX neutral particle fluxes before (the broken line) and after (the solid line) ALEs. (b) The fraction of the enhanced neutral particles fluxes by ALEs. (c) A diagram of the resonant condition under the experimental condition of the shot. The resonance energy region is calculated from 80 to 350 keV.

entire energy range. Therefore it is considered that they are not due to the resonant interaction of energetic ions.

Energetic ion transport due to ALEs, which was described in Sec. 2.3, has been observed in measurements of energy distribution of CX neutral particles from the NDD. Figure 16 shows the time trace of mode amplitude and neutral particle fluxes in the energy windows (a) 20 - 100 keV, (b) 100 - 200 keV, (c) 200 - 300 keV, and (d) 300 - 400 keV during NNB injection, respectively. Here the sampling frequency period is set at 1 ms. Enhancement of CX neutral particle flux with the energy of 100 - 400 keV due to ALEs can be clearly observed. On the other hand, that of 0 - 100 keV is not changed. These results indicate that ALEs cause transport of energetic ions in a limited energy range. Figure 17 (a) shows energy distributions of CX neutral particle flux before the occurrence of ALEs and after the neutral particle flux enhancement due to ALEs, and Fig. 17 (b) shows the enhancement factor of CX neutral particle flux due to ALEs. One can see that the CX neutral particle flux in the energy range of 100 - 370 keV is enhanced due to ALEs. The distribution of the increment in the flux has its peak at ~250 keV. This distribution suggests that the energetic ion transport results from the resonant interaction between energetic ions and ALEs. In order to verify this, we utilize the equation expressed by $N = (f/f_c)\,q - nq + m$, which defines the resonance condition between passing particles and TAE instabilities [34]. Here, f is the mode frequency, f_c is the toroidal transit frequency of the energetic ions, n is the toroidal mode number, m is the poloidal mode number and q is the safety factor. When N is an integer, the resonance condition is satisfied. Figure 17 (c) shows the energy dependence of N around $N = 1$ for the experimental conditions shown at the top of Fig. 17 (c). The shadow area shows the range of the resonant conditions, which is estimated from the width of mode frequency band measured by a Mirnov coil during the ALE and the range of q in the region with the large pressure gradient of energetic ions ($r/a < 0.4$). It is found that the resonant energy range is from 80 to 350 keV for $N = 1$. The energy range of enhanced CX neutral particle flux corresponds qualitatively to the resonant energy range as shown in Fig. 17 (c). This result shows that the enhancement in CX neutral particle flux results from the resonant interaction between energetic ions and ALEs [27].

4. Discussion

As described in Sec. 2.4 and Sec. 3.3, the maximum count rate of the SND and the NDD at the present measurement system are about 1×10^5 cps and about 2×10^5 cps, respectively. The limits of count rate of the SND and the NDD are caused by the analog circuit for the pulse shape discrimination (PSD) and by the fast spectroscopy amplifier, respectively. At higher count rates, their measurements are limited by the pile-up effect. The statistical error of the pulse counting system directly depends on the count rate. However, such a maximum count rate is not sufficient for ITER experiments. For example, the maximum count rate of neutron detectors of the neutron emission profile measurement in ITER needs to be $\sim 10^6$ cps in order to meet the required 10% accuracy. Therefore, upgrade of the maximum count rate of neutron detectors and NDDs is one of the critical issues for ITER experiments.

To overcome this issue, we are developing a digital signal processing (DSP) system for a Stilbene detec-

tor, which will replace the analog PSD system. The DSP technique enables PSD between neutrons and gamma-rays under pile-up conditions. Our new DSP system is based on a Flash ADC (Acquris DC282, 8 G sampling/s). The data acquisition of this system is carried out as follows. Output signals from the photomultiplier anode of the Stilbene crystal scintillator are directly coupled to the Flash ADC and digitized continuously. After the acquisition is completed, the data are transferred to the PC via PCI Bus (133 MB/s). In the PC, PSD between neutrons and gamma-rays is performed using an analyzing software. The PSD method in this system is based on the charge comparison method. The light pulse in the Stilbene detector is comprised of a fast scintillation component (3 - 5 ns) and a slow scintillation component ($\sim$ 400 ns). However, the pulse shape produced by a neutron and a gamma-ray has different time functions. If each pulse is integrated using two different time intervals corresponding to the fast and slow components, the ratio of the integrated charge of fast pulse to that of slow pulse for a neutron is different from that for a gamma-ray. Therefore, a neutron and a gamma-ray can be separated. A performance test of the DSP system has been carried out using neutron and gamma-ray sources, Am-Be and Cf. Shown in Fig. 18 is a 3D plot of separation between neutrons and gamma-rays in $C_F - C_S$ space for a ^{252}Cf source, where C_F and C_S are integrated charges for fast integration interval (25 ns) and slow integration interval (60 ns), respectively, and a color scale is used to indicate the number of events corresponding to a given C_F, C_S set. Since pulses produced by gamma-rays have decay time faster than those produced by neutrons, C_F for gamma-rays (C_{F-G}) is larger than that for neutrons (C_{F-N}) for a certain value of C_S as shown in Fig. 18. The red dashed line shows the border between gamma-ray events and neutron events. Figure 18 shows that the separation between neutrons and gamma-rays can be obtained. Thus, the new DSP system for the Stilbene detector achieves n-γ separation. In future work, after developing the software for n-γ discrimination, this DSP system with the Stilbene crystal scintillator shall be installed in JT-60U to perform neutron measurement with a high sampling rate of $\sim 10^6$ Hz.

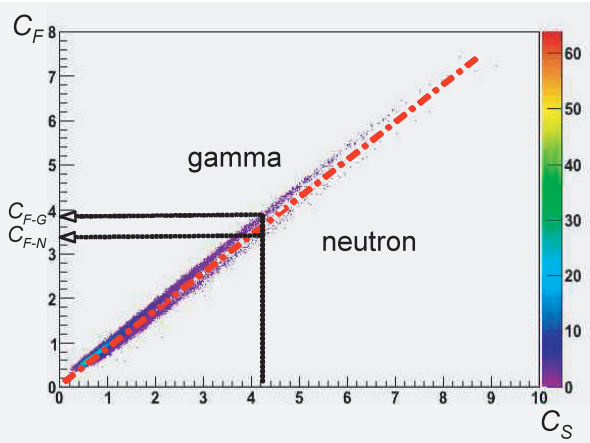

Fig. 18 3D plot of the separation of the neutrons and gamma-rays emitted from a ^{252}Cf source using the DSP system. C_{F-N} and C_{F-G} show integrated charges for fast integration interval for neutrons and gamma-rays, respectively.

5. Summary

The neutron emission profile measurement system and the fast neutral measurement system are developed to analyze behavior and transport of energetic ions due to MHD instabilities in JT-60U.

Line integrated neutron emission profiles are measured using the SNDs, which are installed as the neutron emission profile monitor. The sampling time and/or the aperture sizes of each collimator tube of the neutron emission profile monitor are selected in order that each statistical error is less than 10% and the count rate of each SND is not to exceed the maximum count rate. The sampling rate is set at 10 ms in usual experiments. The collimator sizes of inner channels and of outer channels are also set at 20 mm and at 30 mm, which correspond to the spatial resolution of 20 mm and 30 mm at R = 3.3 m, respectively. Also, the effect of neutron scattering and attenuation in the JT-60U materials, for example the vacuum vessel and the neutron collimator array, is evaluated with MCNP and is taken into account in the measurement of neutrons. The measured neutron profile in the neutral beam heated quiescent plasma is compared with the profile calculated using the TOPICS code. Although there is 30% error in the innermost channel between the measurement and the calculation, there is an agreement within 10% in the other channels. Furthermore, it is found from the measurement of the neuron emission profile that the energetic ions are transported from the core region of the plasma to the outer region due to ALEs, which are the bursting mode in the frequency range of the TAEs induced by NNB injection.

The flux and the energy distribution of fast CX neutral particles are measured with a NDD, which has many favorable characteristics as a radiation detector: compact size, high radiation resistance, high band gap, etc. A n-γ shield is set up around the NDD to reduce neutron and gamma-ray background. Time resolved measurements of the continuous energy distributions of CX neutral particles in the energy range between 20 $\sim$ 500 keV with energy resolution of 1.95 KeV become possible using the NDD. The data sampling frequency period is changed from 10 ms to 1 ms depending on the experimental conditions. Furthermore, to analyze energetic ion transport, fast CX neutral particles are measured in the presence of MHD instabilities. In particular, from the changes in the energy distribution due to ALEs, it is found for the first time that energetic ions are transported through the resonant interaction between energetic ions and ALEs.

A new DSP system for a neutron detector and an NDD

is being developed in order to increase the maximum count rate up to $\sim 10^6$ cps, which is the required maximum count in ITER plasmas. The Stilbene detector is used. Good separation between neutrons and gamma-rays of this DSP system was verified with a performance test using an Am-Be and a Cf neutron/gamma source.

Acknowledgments

The authors would like to thank the JT-60 team for their support and useful discussions. This work was partly supported by a JSPS. Grant-in-Aid for Scientific Research (B) (No.14208056) and by a Grant-in-Aid for Scientific Researches on Priority Areas from Ministry of Education, Culture, Sports, Science and Technology (No.17044009).

[1] R.J. Goldston *et al.*, Phys. Rev. Lett. **47**, 647 (1981).
[2] D.J. Sigmar *et al.*, Phys. Fluids B **4**, 1506 (1992).
[3] ITER Physics Basis Editors. Nucl. Fusion **39**, 2471 (1999).
[4] S. Ide *et al.*, Nucl. Fusion **45**, S48 (2005).
[5] J. Pamela *et al.*, Nucl. Fusion **45**, S63 (2005).
[6] T.C. Luce, Nucl. Fusion **45**, S86 (2005).
[7] M. Kuriyama *et al.*, Fusion Sci. Tech. **42**, 424 (2002).
[8] Y. Kusama *et al.*, Nucl. Fusion **39**, 1837 (1999).
[9] K. Shinohara *et al.*, Nucl. Fusion **41**, 603 (2001).
[10] T. Nishitani *et al.*, Rev. Sci. Instrum. **63**, 5270 (1992).
[11] Y. Kusama *et al.*, Rev. Sci. Instrum. **66**, 339 (1995).
[12] L.C. Johonson *et al.*, Rev. Sci Instrum, **70**, 1145 (1999).
[13] J.M. Adam *et al.*, Nucl. Instrum. Methods. Phys. Res. A **329**, 277 (1993).
[14] A.V Krasilnikov *et al.*, IEEE trans. Nucl. Sci. **45**, 385 (1998).
[15] A.V Krasilnikov *et al.*, J. Plasma. Fusion Res. **75**, 967 (1999).
[16] M. Ishikawa *et al.*, Rev. Sci Instrum. **73**, 4237 (2002).
[17] F.D. Brooks *et al.*, Nucl. Instrum. Methods. **162**, 477 (1979).
[18] T. Nakamura *et al.*, *Proc. Int. Ion Eng. progress-ISIAT* **83**, 567 (1983).
[19] LA-12625-M, edited by J.F. Briesmeister, (Los Alamos National Laboratory, 1997).
[20] H. Shirai *et al.*, J. Phys. Soc. Jpn. **64**, 4209 (1995).
[21] Y. Koide *et al.*, Rev. Sci. Instrum. **72**, 119 (2001).
[22] T. Hatae *et al.*, Rev. Sci. Instrum. **70**, 772 (1999).
[23] K. Kadota *et al.*, Nucl. Fusion **20**, 209 (1980).
[24] T.H. Stix, Plasma Phys. **14**, 367 (1972).
[25] Y. Yamasita, JAERI-M 87-206 (1998).
[26] M. Ishikawa *et al.*, Nucl. Fusion **45**, 1474 (2005).
[27] J.L. Blankenship, IRE Trans. Nucl. Sci. **NS-7**, 190 (1960).
[28] J.H. Kaneko *et al.*, Nucl. Instrum. Methods. Phys. Res. A **505**, 187 (2003).
[29] M. Ishikawa *et al.*, Rev. Sci Instrum. **75**, 3643 (2004).
[30] A. Sykes and J.A. Wesson, Phys. Rev. Lett. **37**, 140 (1976).
[31] F.B. Marcus *et al.*, Nucl. Fusion **34**, 687 (1994).
[32] Ya.I. Kolesnichenko *et al.*, Nucl. Fusion **35**, 1579 (1995).
[33] N. Isei *et al.*, Fusion Eng. Des. **53**, 213 (2001).
[34] R.B. White *et al.*, Phys. Fluids **26**, 2985 (1983).